



Cite this: *Mater. Adv.*, 2025,  
6, 969

## Mn-substitution effects on the magnetic and zero-field ferromagnetic resonance properties of $\epsilon$ -Fe<sub>2</sub>O<sub>3</sub> nanoparticles<sup>†</sup>

Jessica MacDougall, <sup>a</sup> Asuka Namai, <sup>\*a</sup> Onno Strolka <sup>‡,a</sup> and Shin-ichi Ohkoshi <sup>\*ab</sup>

Metal substitution is an important way to tune the magnetic properties of ferrites. In the present study, to investigate the effects of Mn substitution on the magnetic properties and millimeter wave absorption properties on  $\epsilon$ -Fe<sub>2</sub>O<sub>3</sub> for the first time, Mn-substituted epsilon iron oxides,  $\epsilon$ -Mn<sub>x</sub>Fe<sub>2-x</sub>O<sub>3-x/2</sub> ( $x = 0$  (**Mn0**), 0.10 (**Mn1**), and 0.20 (**Mn2**)) were synthesized by sintering iron oxide hydroxide with manganese hydroxide in a silica matrix. Transmission electron microscopy shows particle sizes of  $18.7 \pm 5.8$  nm (**Mn0**),  $19.0 \pm 6.2$  nm (**Mn1**), and  $19.8 \pm 6.7$  nm (**Mn2**). Energy dispersive X-ray spectroscopy confirms a uniform manganese distribution across all particles, while the powder X-ray diffraction patterns demonstrate that  $\epsilon$ -Mn<sub>x</sub>Fe<sub>2-x</sub>O<sub>3-x/2</sub> has an orthorhombic crystal structure with a space group of *Pna2*<sub>1</sub> (e.g., the lattice constants in **Mn2** are  $a = 5.1031(4)$  Å,  $b = 8.7759(8)$  Å, and  $c = 9.4661(7)$  Å). As the Mn substitution ratio increases, the Curie temperature decreases from 487 K (**Mn0**) to 469 K (**Mn2**). As for the magnetic properties at 300 K, the coercive field increases from 17.2 kOe (**Mn0**) to 18.2 kOe (**Mn2**), while the saturation magnetisation decreases from 17.1 emu g<sup>-1</sup> (**Mn0**) to 13.9 emu g<sup>-1</sup> (**Mn2**), with increasing substitution ratio. Terahertz time-domain spectroscopy demonstrates that the samples exhibit electromagnetic wave absorption in the millimetre-wave region, due to zero-field ferromagnetic resonance. As the Mn substitution ratio increases, the resonance frequency increases from 174 GHz (**Mn0**) to 182 GHz (**Mn1**) and 187 GHz (**Mn2**). Due to the substitution of Fe<sup>3+</sup> with Mn<sup>2+</sup>, the saturation magnetisation decreases and the coercive field and the resonance frequency increase.

Received 15th September 2024,  
Accepted 3rd December 2024

DOI: 10.1039/d4ma00927d

rsc.li/materials-advances

## Introduction

The demand for materials capable of absorbing electromagnetic waves has escalated due to recent advances in telecommunication technologies. As millimetre waves (30–300 GHz) become more common in applications such as high-speed wireless communications and radar systems, the development of efficient millimetre-wave absorbing materials is necessary to mitigate noise and interference.<sup>1–6</sup> Electromagnetic wave absorbing materials are categorized by their absorbance mechanism, such as magnetic loss (e.g., spinel ferrites, barium

ferrites) or dielectric loss. Several examples of absorbing materials in the millimetre-wave region have been reported.<sup>7–10</sup> Amongst them, Epsilon iron(III) oxide ( $\epsilon$ -Fe<sub>2</sub>O<sub>3</sub>) shows millimetre-wave absorption at a high frequency of 182 GHz due to its zero-field ferromagnetic resonance.<sup>11–17</sup> Furthermore,  $\epsilon$ -Fe<sub>2</sub>O<sub>3</sub> exhibits a high coercivity, which is retained even with single-digit-diameters.<sup>18–20</sup> Due to its unique functionalities, various other applications in addition to millimetre-wave absorption are anticipated to use  $\epsilon$ -Fe<sub>2</sub>O<sub>3</sub> such as magnetic recording,<sup>21–23</sup> ferroelectric devices,<sup>24–28</sup> magnetic hyperthermia,<sup>29,30</sup> MRI contrast,<sup>31</sup> Li-ion batteries,<sup>32</sup> heavy metal ion detection,<sup>33</sup> and photocatalytic applications.<sup>34</sup> Moreover,  $\epsilon$ -Fe<sub>2</sub>O<sub>3</sub> was recently discovered on the surface of ancient glazed pottery, reportedly playing an important role as a pigment.<sup>35–42</sup> Therefore,  $\epsilon$ -Fe<sub>2</sub>O<sub>3</sub> has been attracting attention, and various synthesis methods have been investigated.<sup>43–56</sup>

Metal substitution can tailor the intrinsic properties of  $\epsilon$ -Fe<sub>2</sub>O<sub>3</sub>. To date,  $\epsilon$ -Fe<sub>2</sub>O<sub>3</sub> has been substituted with gallium,<sup>14,57,58</sup> aluminum,<sup>12,59–61</sup> chromium,<sup>62,63</sup> rhodium,<sup>13,64,65</sup> ruthenium,<sup>66,67</sup> indium,<sup>68,69</sup> and scandium<sup>70</sup> alongside co-substitution with titanium and cobalt.<sup>16,23,71</sup> This approach can attune the coercive field

<sup>a</sup> Department of Chemistry, School of Science, The University of Tokyo, 7-3-1 Hongo, Bunkyo-ku, Tokyo 113-0033, Japan. E-mail: Asuka@chem.s.u-tokyo.ac.jp, Ohkoshi@chem.s.u-tokyo.ac.jp

<sup>b</sup> CNRS International Research Laboratory DYNACOM, 7-3-1 Hongo, Bunkyo-ku, Tokyo 113-0033, Japan

† Electronic supplementary information (ESI) available. CCDC 2380300–2380302. For ESI and crystallographic data in CIF or other electronic format see DOI: <https://doi.org/10.1039/d4ma00927d>

‡ Present address: Institute of Physical and Theoretical Chemistry, The University of Tübingen, Auf der Morgenstelle 18, D-72076 Tübingen, Germany.



and zero-field ferromagnetic resonance. So far, only rhodium and ruthenium substitution have been reported to increase magnetic anisotropy. In the present study, we investigated the effect of manganese substitution, which has not been explored previously. In this paper, we report the synthesis, crystal structure, magnetic properties, and millimetre-wave absorption properties of Mn-substituted  $\epsilon$ -Fe<sub>2</sub>O<sub>3</sub>.

## Results and discussion

### Materials

Fig. 1 shows the synthetic scheme. Varying the feed ratio ( $=[\text{Mn}]/[\text{Mn} + \text{Fe}]$ ) produced three samples: 0 (**Mn0**), 0.05 (**Mn1**), and 0.10 (**Mn2**). Iron oxy-hydroxide ( $\beta$ -FeO(OH)) nanoparticle dispersions and Mn(NO<sub>3</sub>)<sub>2</sub> were added to 0.420 dm<sup>3</sup> water. The molar amounts of Fe ( $n_{\text{Fe}}$ ) in  $\beta$ -FeO(OH) and Mn ( $n_{\text{Mn}}$ ) in Mn(NO<sub>3</sub>)<sub>2</sub> were ( $n_{\text{Fe}}, n_{\text{Mn}} = (10.0, 0 \text{ mmol})$  for **Mn0**, (9.52, 0.51 mmol) for **Mn1**, and (9.02, 1.01 mmol) for **Mn2**). While stirring the solution at 50 °C, aqueous ammonia (25%, 0.0192 dm<sup>3</sup>) was slowly added dropwise. Then the reaction mixture was stirred for an additional 30 minutes. Afterwards, tetraethyl orthosilicate (0.024 dm<sup>3</sup>) was added dropwise. Subsequent stirring at 50 °C for 20 hours yielded a colloidal solution. The addition of ammonium sulphate ( $\sim 10 \text{ g}$  per 0.200 dm<sup>3</sup>) precipitated the product.

The precipitated product was collected, washed by centrifugation, and dried at 60 °C. Next, the precipitate was ground into a fine powder and sintered in air for 4 hours at 1102 °C. The silica matrix was etched using a 5 mol dm<sup>-3</sup> NaOH aqueous solution at 65 °C. Afterwards, the samples were collected by centrifugation, washed with water, and dried, providing a red-brown powder. Elemental analysis was performed with X-ray fluorescence spectroscopy (XRF). Table 1 shows that the observed [Mn]/[Mn + Fe] ratios were consistent with the feed ratios (*i.e.*, 0 for **Mn0**, 0.05 for **Mn1**, and 0.10 for **Mn2**).

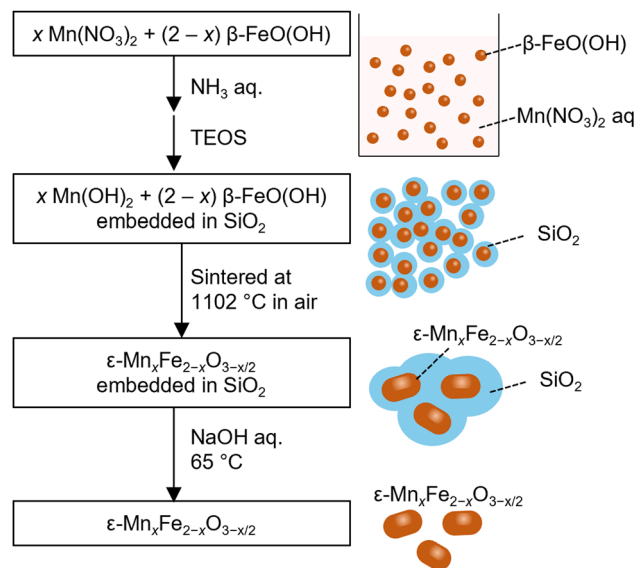


Fig. 1 Schematic of  $\epsilon$ -Mn<sub>x</sub>Fe<sub>2-x</sub>O<sub>3-x/2</sub> nanoparticle synthesis.

Table 1 Feed and experimental [Mn]/[Mn + Fe] ratio

Sample	Feed [Mn]/[Mn + Fe]	Observed [Mn]/[Mn + Fe]
<b>Mn0</b>	0	0
<b>Mn1</b>	0.05	0.05
<b>Mn2</b>	0.10	0.10

Transmission electron microscopy (TEM) images were acquired using a JEM-1011 (JEOL). Fig. 2a shows the TEM images. The samples consisted of nanoparticles with sizes of  $18.7 \pm 5.8 \text{ nm}$  (**Mn0**),  $19.0 \pm 6.2 \text{ nm}$  (**Mn1**), and  $19.8 \pm 6.7 \text{ nm}$  (**Mn2**). Scanning transmission electron microscopy with electron dispersive spectroscopy (STEM-EDS) images were taken with a Thermal ARM-200F. Fig. 2b shows the STEM-EDS images for **Mn1**. The distribution of Mn ions was consistent across all the particles, indicating that Mn was uniformly substituted into the iron oxide structure. Quantitative analysis of individual particles showed that the average [Mn]/[Mn + Fe] in the sample was 0.05 for **Mn1**. This value corresponds to the XRF results (Fig. S1, ESI†).

### Crystal structure and composition analysis

Powder X-ray diffraction (PXRD) measurements were conducted using a Rigaku Ultima IV with  $\text{Cu K}\alpha = 1.5418 \text{ \AA}$  radiation, and Rietveld analyses were performed using Rigaku PDXL2 software. Fig. 3 shows the PXRD patterns of each sample. **Mn0** consisted of  $\epsilon$ -Fe<sub>2</sub>O<sub>3</sub> (96%, orthorhombic, *Pna*2<sub>1</sub> space group) with lattice constants of  $a = 5.0907(4) \text{ \AA}$ ,  $b = 8.7922(8) \text{ \AA}$ ,

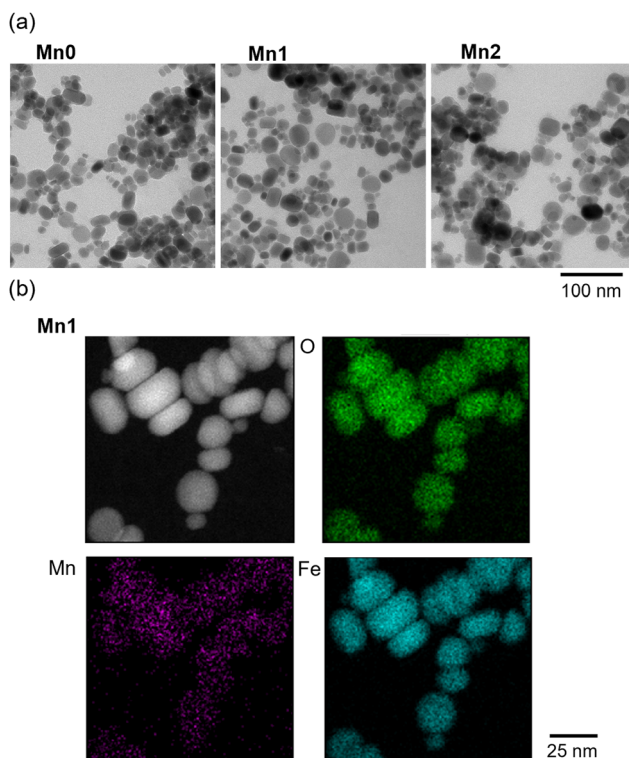
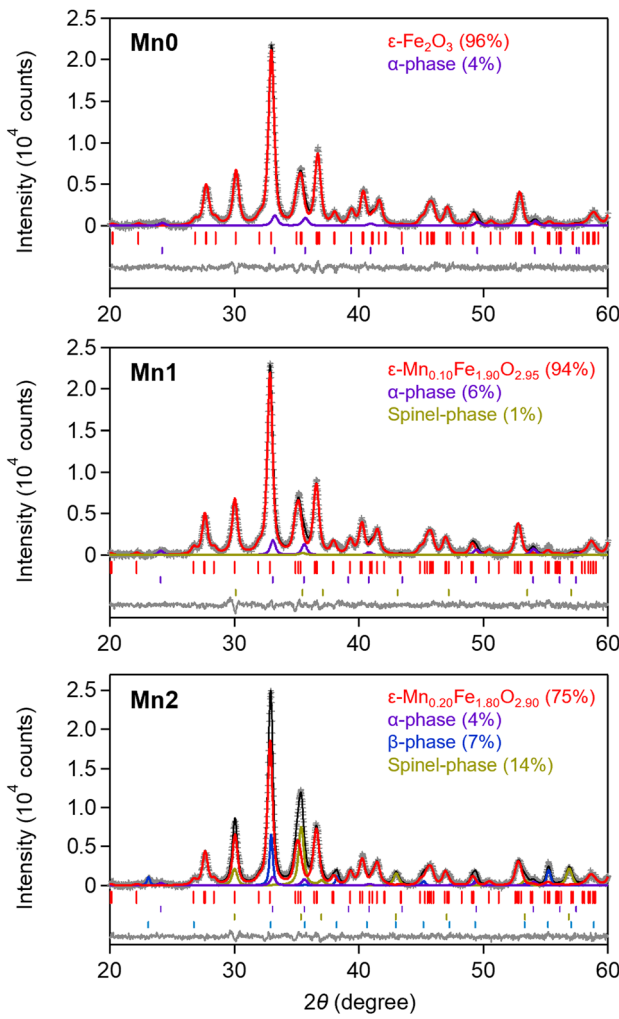


Fig. 2 (a) TEM images of **Mn0**, **Mn1**, and **Mn2**. (b) STEM-EDS images with elemental mapping of **Mn1**.





**Fig. 3** PXRD patterns with Rietveld analyses. Gray crosses, black lines, and grey lines indicate the observed pattern, the calculated pattern, and their difference, respectively. Red, purple, blue, and gold lines denote the calculated patterns for the  $\epsilon$ -phase,  $\alpha$ -phase,  $\beta$ -phase, and spinel-phase, respectively. Red, purple, blue, and gold bars indicate the calculated Bragg positions for the  $\epsilon$ -phase,  $\alpha$ -phase,  $\beta$ -phase, and spinel-phase, respectively.

$c = 9.4764(5)$  Å, and  $V = 424.15(6)$  Å<sup>3</sup> and a small impurity of  $\alpha$ -Fe<sub>2</sub>O<sub>3</sub> (4%, hexagonal,  $R\bar{3}c$  space group). Mn1 was very similar to **Mn0** as it was mostly  $\epsilon$ -phase (94%) and  $\alpha$ -phase (6%). However, there was a small amount of spinel-phase (1%, cubic,  $Fd\bar{3}m$  space group). The major phase of **Mn2** was also  $\epsilon$ -phase (75%) along with smaller amounts of spinel-phase (14%),  $\alpha$ -phase (4%), and  $\beta$ -phase (7%, cubic,  $Ia\bar{3}$  space group). The phase diagram is shown in Fig. S2 (ESI<sup>†</sup>).

The lattice constants changed monotonically with manganese substitution (Fig. 4a and Table S1, ESI<sup>†</sup>). In the  $\epsilon$ -phase,  $a$  increased from  $a = 5.0907(4)$  Å (**Mn0**) to  $5.1031(4)$  Å (**Mn2**), whereas both  $b$  and  $c$  decreased from  $b = 8.7922(8)$  Å (**Mn0**) to  $8.7759(8)$  Å (**Mn2**) and  $c = 9.4764(5)$  Å (**Mn0**) to  $9.4661(7)$  Å (**Mn2**). Since the lattice volume was reduced (*i.e.*, from  $V = 424.15(6)$  Å<sup>3</sup> (**Mn0**) to  $423.93(6)$  Å<sup>3</sup> (**Mn2**)), the  $\epsilon$ -phase showed an anisotropic contraction. X-ray photoelectron

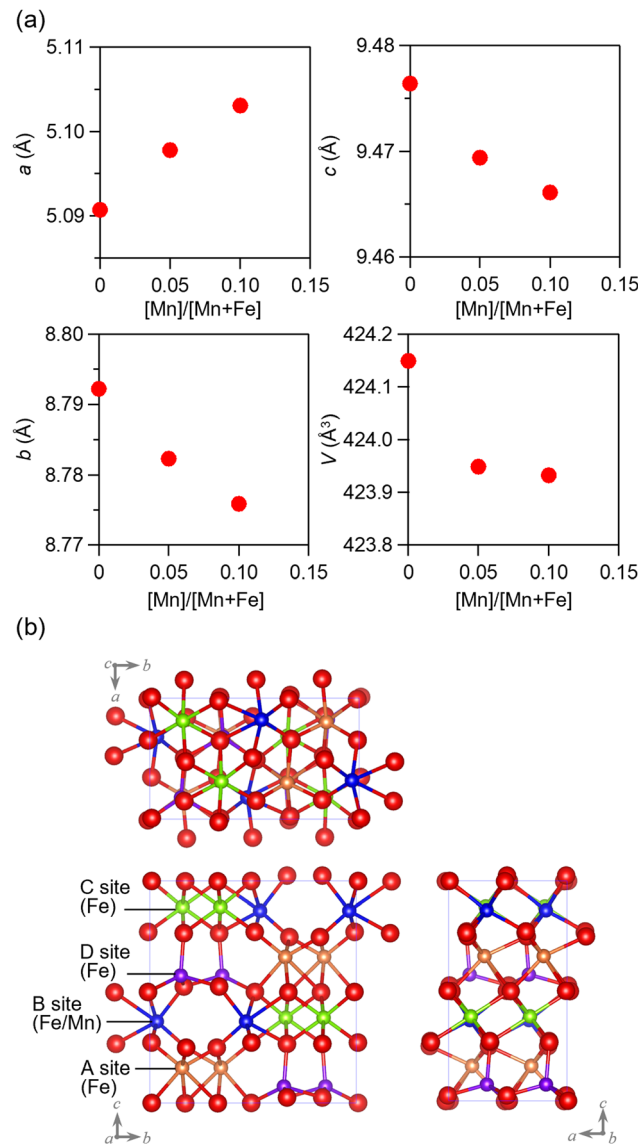


**Fig. 4** (a) Change in lattice parameters of  $\epsilon$ -Mn<sub>x</sub>Fe<sub>2-x</sub>O<sub>3-x/2</sub>. (b) Crystal structure of  $\epsilon$ -Mn<sub>x</sub>Fe<sub>2-x</sub>O<sub>3-x/2</sub>. Orange, blue, purple, and red balls represent metal atoms at the A, B, C, and D sites, and O atoms, respectively.

spectroscopy (XPS) measurements indicated that all samples had a Mn 2p peak at 641 eV. This peak was assigned to Mn<sup>2+</sup>.<sup>72</sup> The change in the lattice constants of the unit cell can be considered as follows: replacing trivalent Fe<sup>3+</sup> ions (ionic radius = 0.645 Å) with divalent Mn<sup>2+</sup> (ionic radius = 0.830 Å) introduced oxygen vacancies into the structure, which anisotropically affected the lattice constants.<sup>73</sup> There are several examples of hematite displaying such a volume contraction.<sup>74–76</sup>

The chemical compositions and corresponding oxygen vacancies for the Mn<sup>2+</sup>-substituted iron oxides were determined by charge balance considerations, assuming that each phase contained the same ratio of Mn<sup>2+</sup> cations. The estimated compositions of each phase were  $\epsilon$ -Fe<sub>2</sub>O<sub>3</sub> (96%) and  $\alpha$ -Fe<sub>2</sub>O<sub>3</sub> (4%) for **Mn0**,  $\epsilon$ -Mn<sub>0.10</sub>Fe<sub>1.90</sub>O<sub>2.95</sub> (94%),  $\alpha$ -Mn<sub>0.10</sub>Fe<sub>1.90</sub>O<sub>2.95</sub> (6%), and spinel-Mn<sub>0.15</sub>Fe<sub>2.85</sub>O<sub>4</sub> (1%) for **Mn1**, and  $\epsilon$ -Mn<sub>0.20</sub>Fe<sub>1.80</sub>O<sub>2.90</sub> (75%),

$\alpha$ -Mn<sub>0.20</sub>Fe<sub>1.80</sub>O<sub>2.90</sub> (4%),  $\beta$ -Mn<sub>0.20</sub>Fe<sub>1.80</sub>O<sub>2.90</sub> (7%), and spinel-Mn<sub>0.30</sub>Fe<sub>2.70</sub>O<sub>4</sub> (14%) for **Mn2**.

Fig. 4b shows the crystal structure of the  $\epsilon$ -Mn<sub>x</sub>Fe<sub>2-x</sub>O<sub>3-x/2</sub>. The structure has four non-equivalent metal sites (*i.e.*, two distorted octahedral sites (A and B sites)), one regular octahedral site (C site), and one tetrahedral site (D site). Rietveld analysis indicated that Mn doping selectively occurred at the distorted octahedral B site. Previous reports on metal-substituted  $\epsilon$ -Fe<sub>2</sub>O<sub>3</sub> indicated that large metal cations (In<sup>3+</sup>; 0.800 Å) substituted into the distorted octahedral A and B sites,<sup>68</sup> while small metal cations (Al<sup>3+</sup>; 0.535 Å, Ga<sup>3+</sup>; 0.620 Å, Ti<sup>4+</sup>; 0.605 Å) substituted into the tetrahedral D sites<sup>12,14,22</sup> and similar size cations (Rh<sup>3+</sup>; 0.665 Å, Ru<sup>3+</sup>; 0.68 Å) substituted into the regular octahedral C sites.<sup>13,64,66</sup> In light of these reports, Mn<sup>2+</sup> was considered to occupy the B site because it has a larger ionic radius than that of Fe<sup>3+</sup>.

### Magnetic properties

Fig. 5 shows the field-cooled magnetisation (FCM) curves under an external field of 1 kOe. The Curie temperatures ( $T_C$ ) were 487 K for **Mn0**, 471 K for **Mn1**, and 469 K for **Mn2**. **Mn1** and **Mn2** had contributions from the spinel-phase (Fig. S3, ESI<sup>†</sup>). Fig. 6a left shows the magnetic hysteresis loops measured at 300 K. The ratio of Mn substitution affected the  $H_c$  value. The value increased slightly from 17.2 kOe for **Mn0** to 17.3 kOe for **Mn1**. However, **Mn2** exhibited a large distortion in the hysteresis loop, which had a negative effect on  $H_c$  (*i.e.*, 0.35 kOe), due to the inclusion of the soft-magnetic spinel-phase.

To estimate the intrinsic  $H_c$  value of  $\epsilon$ -Mn<sub>x</sub>Fe<sub>2-x</sub>O<sub>3-x/2</sub>, we applied a correction that considered the contributions of the spinel-phase and  $\alpha$ -phase (Fig. 6a, right). The estimated  $H_c$  values for  $\epsilon$ -Mn<sub>x</sub>Fe<sub>2-x</sub>O<sub>3-x/2</sub> increased as the Mn ratio increased: 17.2 kOe for  $\epsilon$ -Fe<sub>2</sub>O<sub>3</sub>, 18.0 kOe for  $\epsilon$ -Mn<sub>0.10</sub>Fe<sub>1.90</sub>O<sub>2.95</sub>, and 18.2 kOe for  $\epsilon$ -Mn<sub>0.20</sub>Fe<sub>1.80</sub>O<sub>2.90</sub>. By contrast, the saturation magnetisation ( $M_s$ ) decreased: 17.1 emu g<sup>-1</sup> for  $\epsilon$ -Fe<sub>2</sub>O<sub>3</sub>, 15.6 emu g<sup>-1</sup> for  $\epsilon$ -Mn<sub>0.10</sub>Fe<sub>1.90</sub>O<sub>2.95</sub>, and 13.9 emu g<sup>-1</sup> for  $\epsilon$ -Mn<sub>0.20</sub>Fe<sub>1.80</sub>O<sub>2.90</sub> (Fig. 6b and Table 2).

### Millimetre wave absorption properties

An Advantest TAS7400 was used to perform terahertz time-domain spectroscopy (THz-TDS) measurements. A THz pulse was irradiated onto the sample and both the transmitted and reflected THz pulses were measured in the time domain. The spectra were obtained by a Fourier transformation. The measurement employed pellet samples (13 mmφ). The pellets had a thickness ( $d$ ) of approximately 1.11 mm and a volume filling ratio of 54 vol%. Fig. 7 shows the absorption spectra with the fringe patterns arising from multiple reflections removed.<sup>77</sup> As the Mn substitution ratio increased, the absorption peak shifted to higher frequencies, the resonance frequency ( $f_r$ ) increased from 174 GHz (**Mn0**) to 182 GHz (**Mn1**) and 187 GHz (**Mn2**), and the full width at half maximum (FWHM) broadened from 9 GHz (**Mn0**) to 11 GHz (**Mn1**) and 13 GHz (**Mn2**). The observed increase in the  $f_r$  value is apparently due to Mn-substitution since the  $f_r$  value of  $\epsilon$ -Fe<sub>2</sub>O<sub>3</sub>, which can be slightly affected by particle size and shape, is 182 GHz at most.

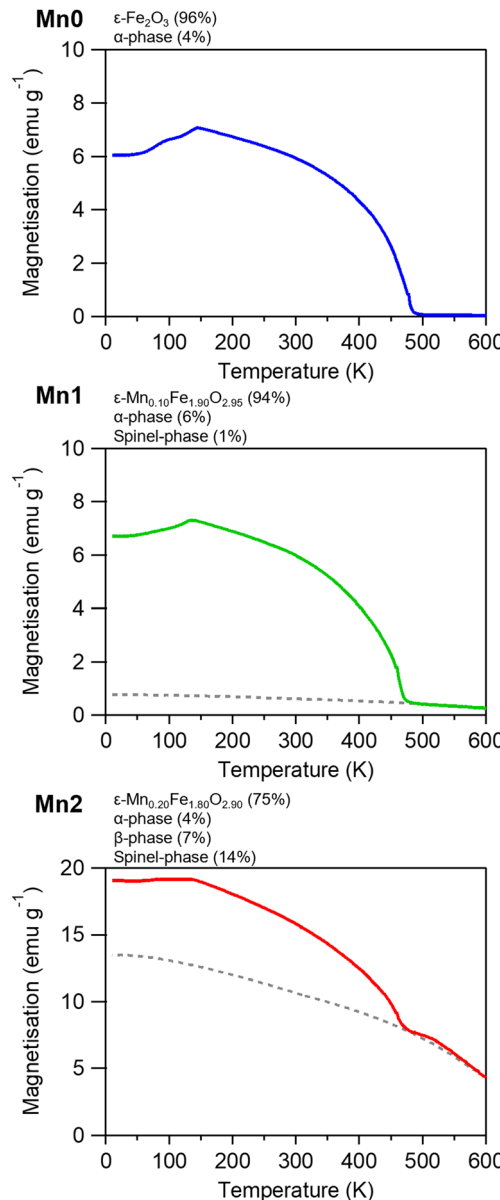


Fig. 5 FCM curves in an external field of 1 kOe for **Mn0**, **Mn1**, and **Mn2**. Dotted line is to guide the eye for the contribution of the spinel-phase.

A similar increase of  $f_r$  in metal-substituted  $\epsilon$ -Fe<sub>2</sub>O<sub>3</sub> has only been reported with rhodium substitution.

### Mechanism for the increased resonance frequency and coercive field by manganese substitution

In the present manganese substituted  $\epsilon$ -Fe<sub>2</sub>O<sub>3</sub>, XPS measurements confirmed that Fe<sup>3+</sup> was replaced by Mn<sup>2+</sup>. O<sup>2-</sup> vacancies maintained the electrical neutrality. Therefore, the composition was  $\epsilon$ -Mn<sub>x</sub>Fe<sub>2-x</sub>O<sub>3-x/2</sub>. The O<sup>2-</sup> vacancies reduced the number of superexchange interaction pathways, decreasing the  $T_C$  value.<sup>78-80</sup> In addition, B-site substitution of Mn<sup>2+</sup> affected the magnetic structure of  $\epsilon$ -Fe<sub>2</sub>O<sub>3</sub>.  $\epsilon$ -Fe<sub>2</sub>O<sub>3</sub> is a collinear ferrimagnet composed of positive sublattice magnetisations at B and C sites ( $M_B$  and  $M_C$ ) and negative sublattice



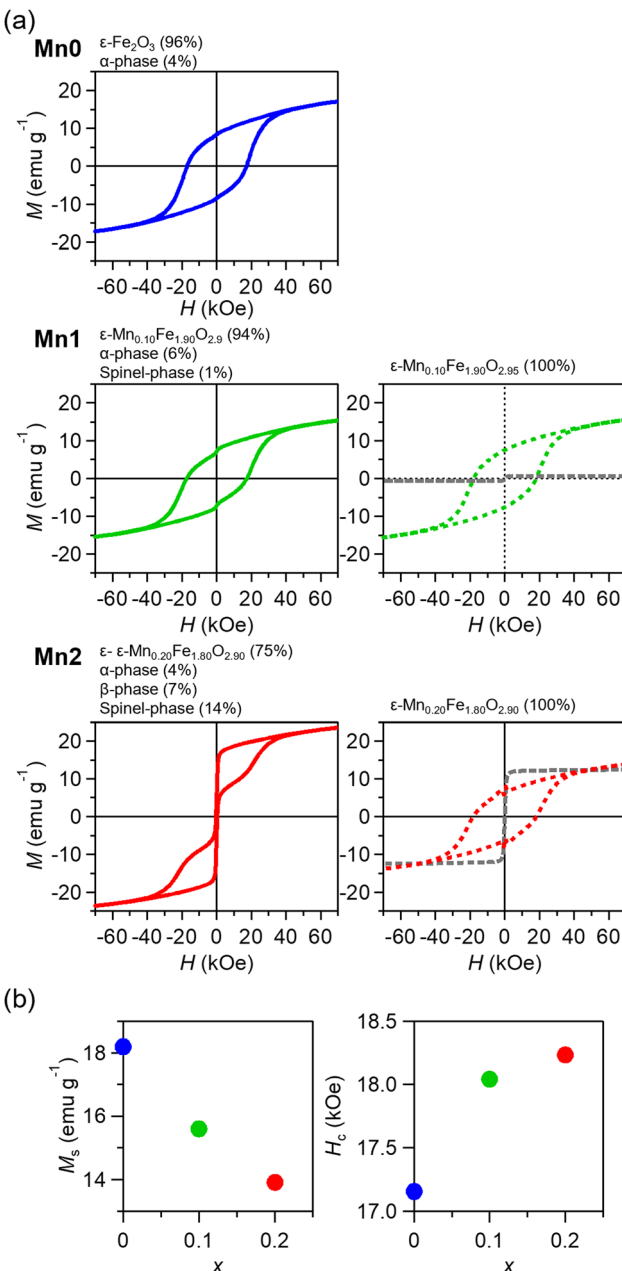


Fig. 6 (a) Magnetisation versus external magnetic field curves at 300 K for (left) observed and (right) estimated curves. Coloured and grey lines represent the curve for the contributions of the  $\epsilon$ -Mn<sub>x</sub>Fe<sub>2-x</sub>O<sub>3-x/2</sub> and spinel-phase, respectively. (b)  $M_s$  and  $H_c$  versus  $x$  plot.

Table 2 Magnetic properties of  $\epsilon$ -Mn<sub>x</sub>Fe<sub>2-x</sub>O<sub>3-x/2</sub>

Sample	$T_c$ (K)	$H_c$ (kOe)	$M_s$ (emu g⁻¹)
Mn0	487	17.2	17.1
Mn1	471	18.0	15.6
Mn2	469	18.2	13.9

magnetisations at A and D sites ( $M_A$  and  $M_D$ ).<sup>81–83</sup> Since the superexchange interaction at tetrahedral D sites was smaller than those at the other octahedral sites (A–C sites),  $M_D$  was smaller than the other sublattice magnetisation. Consequently,

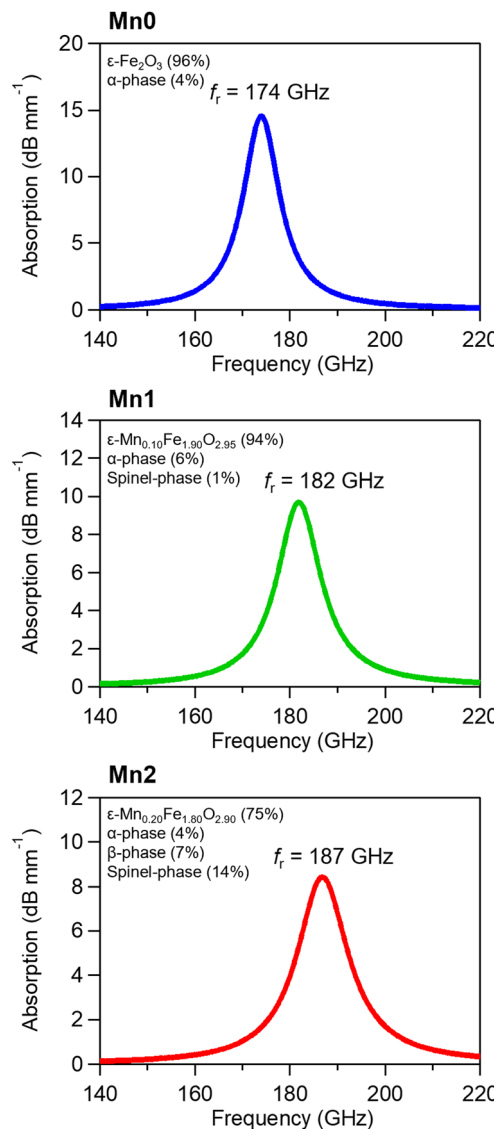


Fig. 7 Millimetre-wave absorption spectra of Mn0, Mn1, and Mn2 normalized by the  $\epsilon$ -phase fraction and filling ratio. Fringe patterns from multiple reflections are removed.

sublattice magnetisations did not compensate for each other and spontaneous magnetisation appeared in  $\epsilon$ -Fe<sub>2</sub>O<sub>3</sub>. Mn<sup>2+</sup> substitution at the B sites causes O<sup>2-</sup> vacancies around the substituted B sites, which reduced the number of superexchange interaction pathways and decreased  $M_B$ . As a result, the total magnetisation decreased, which was experimentally observed by the 19% decrease in saturation magnetisation. On the other hand, the magnetic anisotropy  $H_a$  tended to be inversely proportional to magnetisation, while the coercive field and resonance frequency were proportional to  $H_a$ .<sup>84</sup> Due to the decreased magnetisation, the coercive field and the resonance frequency increased by 7% and 8%, respectively.

## Conclusions

We prepared a series of Mn-substituted  $\epsilon$ -Fe<sub>2</sub>O<sub>3</sub>, and  $\epsilon$ -Mn<sub>x</sub>Fe<sub>2-x</sub>O<sub>3-x/2</sub> ( $x = 0, 0.1$ , and  $0.2$ ). Replacing trivalent Fe<sup>3+</sup> ions with divalent Mn<sup>2+</sup>

ions forms oxygen vacancies, causing anisotropic contraction of the unit cell. Mn-substitution increases not only the coercive field from 17.2 kOe ( $x = 0$ ) to 18.2 kOe ( $x = 0.20$ ) but also the zero-field ferromagnetic resonance frequency from 174 GHz ( $x = 0$ ) to 187 GHz ( $x = 0.20$ ). Although Rh-substituted  $\epsilon$ -Fe<sub>2</sub>O<sub>3</sub> shows a similar increase in the resonance frequency and coercive field, the mechanism differs from the present material. The enhancement in Rh-substituted  $\epsilon$ -Fe<sub>2</sub>O<sub>3</sub> is caused by the orbital angular momentum on Rh<sup>3+</sup>.<sup>13</sup> From the viewpoint of sustainable development goals, manganese is the 12th most naturally abundant chemical element in the earth's crust (0.1 wt%). By contrast, rhodium is extremely rare (<0.001 wt%).<sup>85</sup> Consequently, the present material has potential as an eco-friendly material in various applications such as millimetre-wave absorption, magnetic recordings, two-dimensional ferroelectric-ferroelectricity, and biomedical applications.

## Data availability

Crystallographic data for  $\epsilon$ -Mn<sub>x</sub>Fe<sub>2-x</sub>O<sub>3-x/2</sub>, has been deposited at the Cambridge Crystallographic Data Centre under 2380300 – 2380302 and can be obtained from <https://www.ccdc.cam.ac.uk/>. The data supporting this article have been included as part of the ESI.†

## Conflicts of interest

There are no conflicts to declare.

## Acknowledgements

This work was supported in part by a Grant-in-Aid for Scientific Research A from the Japan Society for the Promotion of Science (JSPS) (Grant Number 20H00369), a Grant-in-Aid for Scientific Research B from JSPS (Grant Numbers 23H01920 and 22H02046). We recognize the Cryogenic Research Center at The University of Tokyo, DOWA Technofund, the Tokyo Ohka Foundation for The Promotion of Science and Technology and the Center for Nano Lithography & Analysis at The University of Tokyo. We are grateful to Dr Marie Yoshiyuki at the University of Tokyo, and Dr Yasuto Miyamoto and Mr Kenji Sakane at DOWA Electronics Ltd., for their helpful discussions and for providing the TEM images.

## Notes and references

- Y. Yan, G. Xie, M. P. J. Lavery, H. Huang, N. Ahmed, C. Bao, Y. Ren, Y. Cao, L. Li, Z. Zhao, A. F. Molisch, M. Tur, M. J. Padgett and A. E. Willner, *Nat. Commun.*, 2014, **5**, 4876.
- S. Rangan, T. Rappaport and E. Erkip, *Proc. IEEE*, 2024, **102**, 366–385.
- S. Koenig, D. Lopez-Diaz, J. Antes, F. Boes, R. Henneberger, A. Leuther, A. Tessmann, R. Schmogrow, D. Hillerkuss, R. Palmer, T. Zwick, C. Koos, W. Freude, O. Ambacher, J. Leuthold and I. Kallfass, *Nat. Photonics*, 2013, **7**, 977–981.
- A. Kumar, M. Gupta and R. Singh, *Nat. Photon.*, 2021, **15**, 715–716.
- S. Dang, O. Amin, B. Shihada and M. Alouini, *Nat. Electron.*, 2020, **3**, 20–29.
- J. Jornet, E. Knightley and D. Mittleman, *Nat. Commun.*, 2023, **14**, 841.
- A. Goldman, *Modern Ferrite Technology*, Springer, New York, 2006.
- S. Pawar, S. Biswas, G. Kar and S. Bose, *Polymer*, 2016, **84**, 398–419.
- A. Charles, A. Rider, S. Brown and C. Wang, *Prog. Mater. Sci.*, 2021, **115**, 10075.
- M. Qin, L. Zhang and H. Wu, *Adv. Sci.*, 2022, **9**, 2105553.
- J. Tuček, R. Zbořil, A. Namai and S. Ohkoshi, *Chem. Mater.*, 2010, **22**, 6483–6505.
- A. Namai, S. Sakurai, M. Nakajima, T. Suemoto, K. Matsumoto, M. Goto, S. Sasaki and S. Ohkoshi, *J. Am. Chem. Soc.*, 2009, **131**, 1170–1173.
- A. Namai, M. Yoshiyuki, K. Yamada, S. Sakurai, T. Goto, T. Yoshida, T. Miyazaki, M. Nakajima, T. Suemoto, H. Tokoro and S. Ohkoshi, *Nat. Commun.*, 2012, **3**, 1035.
- S. Ohkoshi, S. Kuroki, S. Sakurai, K. Matsumoto, K. Sato and S. Sasaki, *Angew. Chem., Int. Ed.*, 2007, **46**, 8392–8395.
- G. Jo, M. Yun, Y. Hun Son, B. Park, J. Lee, Y. Kim, Y. Son and Y. Baek, *Chem. Commun.*, 2022, **58**, 11442–11445.
- R. Kinugawa, K. Imoto, Y. Futakawa, S. Shimizu, R. Fujiwara, M. Yoshiyuki, A. Namai and S. Ohkoshi, *Adv. Eng. Mater.*, 2021, **23**, 2001473.
- E. Gorbachev, M. Soshnikov, M. Wu, L. Alyabyeva, D. Myakishev, E. Kozlyakova, V. Lebedev, E. Anokhin, B. Gorshunov, O. Brylev, P. Kazin and L. Trusov, *J. Mater. Chem. C*, 2021, **9**, 6173–6179.
- J. Jin, S. Ohkoshi and K. Hashimoto, *Adv. Mater.*, 2004, **16**, 48–51.
- S. Ohkoshi, A. Namai, K. Imoto, M. Yoshiyuki, W. Tarora, K. Nakagawa, M. Komine, Y. Miyamoto, T. Nasu, S. Oka and H. Tokoro, *Sci. Rep.*, 2015, **5**, 14414.
- M. Gich, C. Frontera, A. Roig, E. Taboada, E. Molins, H. R. Rechenberg, J. D. Ardisson, W. A. A. Macedo, C. Ritter, V. Hardy, J. Sort, V. Skumryev and J. Nogués, *Chem. Mater.*, 2006, **18**, 3889–3897.
- S. Ohkoshi, M. Yoshiyuki, K. Imoto, K. Nakagawa, A. Namai, H. Tokoro, Y. Yahagi, K. Takeuchi, F. Jia, S. Miyashita, M. Nakajima, H. Qiu, K. Kato, T. Yamaoka, M. Shirata, K. Naoi, K. Yagishita and H. Doshita, *Adv. Mater.*, 2020, **32**, 2004897.
- S. Ohkoshi, A. Namai, M. Yoshiyuki, K. Imoto, K. Tamazaki, K. Matsuno, O. Inoue, T. Ide, K. Masada, M. Goto, T. Goto, T. Yoshida and T. Miyazaki, *Angew. Chem., Int. Ed.*, 2016, **55**, 11403.
- T. Jussila, A. Philip, J. Lindén and M. Karppinen, *Adv. Eng. Mater.*, 2023, **25**, 2201262.
- M. Gich, I. Fina, A. Morelli, F. Sánchez, M. Alexe, J. Gàzquez, J. Fontcuberta and A. Roig, *Adv. Mater.*, 2014, **26**, 4645–4652.
- T. Wang, W. Xue, H. Yang, Y. Zhang, S. Cheng, Z. Fan, R.-W. Li, P. Zhou and X. Xu, *Adv. Mater.*, 2024, 2311041.



26 Y. Hamasaki, S. Yasui, T. Katayama, T. Kiguchi, S. Sawai and M. Itoh, *Appl. Phys. Lett.*, 2021, **119**, 182904.

27 Y. Wang, P. Wang, H. Wang, B. Xu, H. Li, M. Cheng, W. Feng, R. Du, L. Song, X. Wen, X. Li, J. Yang, Y. Cai, J. He, Z. Wang and J. Shi, *Adv. Mater.*, 2023, **35**, 2209465.

28 V. Tiron, R. Jijie, I. Dumitru, N. Cimpoesu, I. Burducea, D. Iancu, A. Borhan, S. Gurlui and G. Bulai, *Ceram. Int.*, 2023, **49**, 20304–20314.

29 Y. Gu, M. Yoshiakiyo, A. Namai, D. Bonvin, A. Martinez, R. Piñol, P. Téllez, N. J. O. Silva, F. Ahrentorp, C. Johansson, J. Marco-Brualla, R. Moreno-Loshuertos, P. Fernández-Silva, Y. Cui, S. Ohkoshi and A. Millán, *RSC Adv.*, 2020, **10**, 28786–28797.

30 Y. Gu, N. J. O. Silva, M. Yoshiakiyo, A. Namai, R. Piñol, G. Maurin-Pasturel, Y. Cui, S. Ohkoshi, A. Millán and A. Martinez, *Chem. Commun.*, 2021, **57**, 2285–2288.

31 L. Kubíčková, P. Brázda, M. Veverka, O. Kaman, V. Herynek, M. Vosmanská, P. Dvořák, K. Bernášek and J. Kohout, *J. Magn. Magn. Mater.*, 2019, **480**, 154–163.

32 D. Li, J. Liang, S. Song and L. Li, *ACS Appl. Nano Mater.*, 2023, **6**, 2356–2365.

33 D. Singh, S. Shaktawat, S. K. Yadav, R. Verma, K. R. B. Singh and J. Singh, *Int. J. Biol. Macromol.*, 2024, **265**, 130867.

34 G. Carraro, C. Maccato, A. Gasparotto, T. Montini, S. Turner, O. I. Lebedev, V. Gombac, G. Adami, G. Van Tendeloo, D. Barreca and P. Fornasiero, *Adv. Funct. Mater.*, 2014, **24**, 372–378.

35 S. Tao, Y. Zhu, S. Liu, J. Dong, Y. Yuan and Q. Li, *Crystals*, 2023, **13**, 632.

36 G. Li, Z. Wang, J. Zhou, B. Kang, Y. Ding, M. Guan, X. Wei and Y. Lei, *Herit. Sci.*, 2023, **11**, 58.

37 C. Holé, M. Brunet, B. Joulié, Z. Ren, T. Wang, G. Wallez and P. Sciau, *J. Appl. Crystallogr.*, 2024, **57**, 431–439.

38 M. Guan, Y. Guo, B. Kang, M. Wang, G. Li, Y. Zheng, Y. Ding, M. Wang, N. Wood, Y. Lei, X. Wei and D. Ma, *J. Am. Ceram. Soc.*, 2024, **107**, 522–533.

39 Z. Li, J. Liu, X. Jiang and J. Cui, *J. Eur. Ceram. Soc.*, 2024, **44**, 1856–1863.

40 T. Wang, S. Xia, F. Wang, Z. Ren, P. Sciau, C. Yang, J. Zhu, H. Luo, Q. Li and X. Fu, *J. Eur. Ceram. Soc.*, 2024, **44**, 3337–3343.

41 C. Holé, Z. Ren, F. Wang, J. Zhu, T. Wang and P. Sciau, *Mater. Today Commun.*, 2022, **33**, 104329.

42 Y. Kusano, H. Nakata, Z. Peng, R. S. S. Maki, T. Ogawa and M. Fukuhara, *ACS Appl. Mater. Interfaces*, 2021, **13**, 38491–38498.

43 H. Tokoro, W. Tarora, A. Namai, M. Yoshiakiyo and S. Ohkoshi, *Chem. Mater.*, 2018, **30**, 2888–2894.

44 L. Altenschmidt, P. Beaunier, A. Bordage, E. Rivière, G. Fornasieri and A. Bleuzen, *ChemNanoMat*, 2023, **9**, e202200469.

45 I. Khan, S. Morishita, R. Higashinaka, T. D. Matsuda, Y. Aoki, E. Kuzmann, Z. Homonnay, S. Katalin, L. Pavić and S. Kubuki, *J. Magn. Magn. Mater.*, 2021, **538**, 168264.

46 J. MacDougall, H. Tokoro, M. Yoshiakiyo, A. Namai and S. Ohkoshi, *Eur. J. Inorg. Chem.*, 2024, e202400148.

47 Y. Zhao and G. Wen, *J. Magn. Magn. Mater.*, 2020, **512**, 167039.

48 S. Sakurai, A. Namai, K. Hashimoto and S. Ohkoshi, *J. Am. Chem. Soc.*, 2009, **131**, 18299–18303.

49 M. Tadic, I. Milosevic, S. Kralj, D. Hanzel, T. Barudzija, L. Motte and D. Makovec, *Acta Mater.*, 2020, **188**, 16–22.

50 J. MacDougall, A. Namai, M. Yoshiakiyo and S. Ohkoshi, *Chem. Lett.*, 2023, **52**, 229–232.

51 L. Corbellini, C. Lacroix, C. Harnagea, A. Korinek, G. A. Botton, D. Ménard and A. Pignolet, *Sci. Rep.*, 2017, **7**, 3712.

52 S. Chen, Y. Jiang, T. Yao, A. Tao, X. Yan, F. Liu, C. Chen, X. Ma and H. Ye, *Micron*, 2022, **163**, 103359.

53 S. Suturin, P. Dvortsova, L. Snigirev, V. Ukleev, T. Hanashima, M. Rosado and B. Ballesteros, *Mater. Today Commun.*, 2022, **33**, 104412.

54 J. Yuan, A. Balk, H. Guo, Q. Fang, S. Patel, X. Zhao, T. Terlier, D. Natelson, S. Crooker and J. Lou, *Nano Lett.*, 2019, **19**, 3777–3781.

55 T. Amrillah, L. T. Quynh, C. N. Van, T. H. Do, E. Arenholz, J.-Y. Juang and Y.-H. Chu, *ACS Appl. Mater. Interfaces*, 2021, **13**, 17006–17012.

56 J. Cleron, A. A. Baker, T. Nakotte, A. Troksa and J. Han, *J. Phys. Chem. C*, 2022, **126**, 7256–7263.

57 L. Kubíčková, O. Kaman, P. Veverka, V. Herynek, P. Brázda, K. Bernášek, M. Veverka and J. Kohout, *J. Alloys Compd.*, 2021, **856**, 158187.

58 T. Katayama, S. Yasui, Y. Hamasaki and M. Itoh, *Appl. Phys. Lett.*, 2017, **110**, 212905.

59 L. Kubíčková, O. Kaman, P. Veverka, V. Herynek, P. Brázda, M. Vosmanská, T. Kmječ, P. Dvořák, D. Kubániová and J. Kohout, *Colloids Surf. A*, 2020, **589**, 124423.

60 L. Corbellini, C. Lacroix, D. Ménard and A. Pignolet, *Scr. Mater.*, 2017, **140**, 63–66.

61 Q. Fu and G. Wen, *J. Magn. Magn. Mater.*, 2023, **570**, 170500.

62 Z. Ma, A. Romaguera, F. Fauth, J. Herrero-Martín, J. L. García-Muñoz and M. Gich, *J. Magn. Magn. Mater.*, 2020, **506**, 166764.

63 R. Nickel, C. Sun, D. Motta Meira, P. Shafer and J. van Lierop, *Phys. Rev. Mater.*, 2024, **8**, 024407.

64 S. Ohkoshi, K. Imoto, A. Namai, S. Anan, M. Yoshiakiyo and H. Tokoro, *J. Am. Chem. Soc.*, 2017, **139**, 13268–13271.

65 S. Yasui, T. Katayama, T. Osakabe, Y. Hamasaki, T. Taniyama and M. Itoh, *J. Ceram. Soc. Jpn.*, 2019, **127**, 474–477.

66 A. Namai and S. Ohkoshi, *Eur. J. Chem.*, 2018, **24**, 11880–11884.

67 A. Tamm, A. Tarre, J. Kozlova, M. Rähn, T. Jõgiaas, T. Kahro, J. Link and R. Stern, *RSC Adv.*, 2021, **11**, 7521–7526.

68 S. Sakurai, S. Kuroki, H. Tokoro, K. Hashimoto and S. Ohkoshi, *Adv. Funct. Mater.*, 2007, **17**, 2278–2282.

69 M. Yoshiakiyo, A. Namai, M. Nakajima, K. Yamaguchi, T. Suemoto and S. Ohkoshi, *J. Appl. Phys.*, 2014, **115**, 172613.

70 M. Polášková, O. Malina, J. Tuček and P. Jakubec, *Nanoscale*, 2022, **14**, 5501–5513.

71 S. Ohkoshi, K. Imoto, A. Namai, M. Yoshiakiyo, S. Miyashita, H. Qiu, S. Kimoto, K. Kato and M. Nakajima, *J. Am. Chem. Soc.*, 2019, **141**, 1775–1780.



72 J. Moulder, W. Stickle, P. Sobol and K. Bomben, *Handbook of X-ray Photoelectron Spectroscopy*, PerkinElmer Corporation, Minnesota, 1992.

73 R. Shannon, *Acta Crystallogr.*, 1976, **32**, 751.

74 D. Varshney and A. Yogi, *J. Mol. Struct.*, 2011, **995**, 157–162.

75 P. Kumar, V. Sharma, J. P. Singh, A. Kumar, S. Chahal, K. Sachdev, K. H. Chae, A. Kumar, K. Asokan and D. Kanjilal, *J. Magn. Magn. Mater.*, 2019, **489**, 165398.

76 V. Sahoo, R. N. Bhowmik and S. Khan, *Mater. Chem. Phys.*, 2023, **296**, 127298.

77 A. Namai, Y. Oki, K. Imoto, H. Tokoro and S. Ohkoshi, *J. Mater. Chem. C*, 2022, **10**, 10815–10822.

78 Y. J. Song, G. B. Turpin, R. E. Bornfreund, H. Aoyama and P. E. Wigen, *J. Magn. Magn. Mater.*, 1996, **154**, 37–53.

79 S. Kumari, N. Mottaghi, C. Huang, R. Trappen, G. Bhandari, S. Yousefi, G. Cabrera, M. Seehra and M. Holcomb, *Sci. Rep.*, 2020, **10**, 3659.

80 A. Harbi, A. Azouaoui, S. Benmokhtar and M. Moutaabbid, *J. Supercond. Novel Magn.*, 2022, **35**, 1405–1412.

81 R. Nickel, J. Gibbs, J. Burgess, P. Shafer, D. M. Meira, C. Sun and J. Van Lierop, *Nano Lett.*, 2023, **23**, 7845–7851.

82 M. Yoshikiyo, K. Yamada, A. Namai and S. Ohkoshi, *J. Phys. Chem. C*, 2012, **116**, 8688–8691.

83 S. Ohkoshi, A. Namai and S. Sakurai, *J. Phys. Chem. C*, 2009, **113**, 11235–11238.

84 S. Chikazumi, *Physics of Ferromagnetism*, Oxford University Press, New York, 1997.

85 A. Yaroshevsky, *Geochem. Int.*, 2006, **44**, 48–55.

